PHYSICAL REVIEW B **105**, 224413 (2022)

Editors' Suggestion

Band filling effects on the emergence of magnetic skyrmions: Pd/Fe and Pd/Co bilayers on Ir(111)

I. P. Miranda,[1,2,*] A. B. Klautau,[3] A. Bergman,[2] and H. M. Petrilli[1]

[1]*Instituto de Física, Universidade de São Paulo, Rua do Matão 1371, 05508-090 São Paulo, São Paulo, Brazil*
[2]*Department of Physics and Astronomy, Uppsala University, Box 516, 75120 Uppsala, Sweden*
[3]*Faculdade de Física, Universidade Federal do Pará, CEP 66075-110, Belém, Pará, Brazil*

(Received 17 February 2022; revised 9 April 2022; accepted 9 May 2022; published 21 June 2022)

Structurally similar transition metal systems can have widely differing magnetic properties. A prime example of this is found for bilayers on Ir(111), where the Pd/Fe/Ir(111) ground state has a well-established noncollinear spin texture, while Pd/Co/Ir(111) presents a ferromagnetic (FM) single domain. To unravel the origins of these different magnetic behaviors, an investigation of Pd/Fe and Pd/Co bilayers on Ir(111) is here performed. Based on the obtained *ab initio* electronic structure, exchange coupling parameters J_{ij}, and Dzyaloshinskii-Moriya interactions (DMIs), we demonstrate that, although in Pd/Co/Ir(111) the DMI is significant, two ingredients play a key role in the origin of noncollinearity in Pd/Fe/Ir(111): the presence of magnetic frustrations and a much more in-plane DMI, both with a long-range influence. The J_{ij} and DMI behaviors in both systems can be explained in terms of a simple rigid-band-like model. Also, by performing spin-dynamics simulations with the magnetic parameters tuned from the Pd/Co/Ir(111) to Pd/Fe/Ir(111) *ab initio* values, we could find conditions for the emergence of skyrmionic phases in the originally FM Pd/Co/Ir(111).

DOI: 10.1103/PhysRevB.105.224413

I. INTRODUCTION

Among the manifestations of nanoscale magnetism, one of high interest is the phenomenon of noncollinear magnetism, characterized by magnetic moments of neighboring atoms with no unique quantization axis. Although the nature of this kind of magnetic configuration in solid-state systems is not completely understood on a microscopic level, many different expressions of noncollinear magnetism have been found by the joint effort of experimental and theoretical investigations: parity effects [1,2], vortexlike magnetic structures [3,4], complex spin textures [5–9], and skyrmions [10–14]. The observation of skyrmions [13] in magnetic materials has attracted attention due to their potential applications in novel spintronic technologies, such as logical [15] and nonvolatile [16] data storage devices.

Different materials have been investigated inspecting the possibility of exhibiting noncollinear configurations and, in particular, skyrmions. Those which are constituted by magnetic overlayers on high-spin-orbit coupling (high-SOC) substrates are often good candidates as skyrmionic systems [12,17,18], due to the combination of different exchange mechanisms, such as the Dzyaloshinskii-Moriya interaction (DMI) [19,20], magnetic frustrations [6,21–23], substrate and overlayers hybridizations [24], and even higher-order interactions (e.g., four-spin) [17].

Examples of complex magnetism in atomically thin layers and at interfaces can be found by theoretical studies and measurements, e.g., the extensively investigated Pd/Fe bilayer on Ir(111) [12,25], as well as by decorating the film edge with Fe/Co spots [26]. In this system, the ground state is characterized by a spin-spiral configuration [27,28], and when subjected to the action of an external perpendicular magnetic field [12,25,29–31] (of ∼1–1.5 T and at low temperatures), the emergence of a skyrmion lattice can be observed. As a substrate, the 5*d* element Ir is particularly interesting since the SOC should be significant, which, in conjunction with a low-symmetry situation provided by the surface, leads to an important DMI. In addition, 4*d* elements such as Pd are particularly attractive for use as overlayers, since large magnetic moments can be induced, due to their high magnetic susceptibility. However, if the Fe layer is replaced by Co (periodic table Fe row nearest-neighbor element) to generate Pd/Co/Ir(111), the system presents a ferromagnetic (FM) single-domain state [32].

On one hand, the local magnetic properties of the Pd/Co bilayer on Ir(111) have not yet been deeply investigated by theoretical approaches. In order to understand the microscopic origins and favorable conditions for the emergence of noncollinear magnetism, in special skyrmions [33], a full comparison of Pd/Fe/Ir(111) and Pd/Co/Ir(111) offers a special opportunity, through the analysis of the exchange coupling parameter J_{ij} and the DMI, to discuss the role of each type of interaction. On the other hand, recent studies [34–38] have shown that, even in the absence of favorable intrinsic DMI and frustrated exchange interactions, such properties can be tuned by external or internal modifications in the systems, such as the application of long-term [34,35,38,39]

---

[*] Corresponding author: ivan.miranda@alumni.usp.br

or short-term [37] electric fields or strain [36], or even by introducing defects with strong spin-orbit coupling [7]. In view of that electronic-structure-level controlling of magnetic interactions, one can conjecture that, for given appropriate conditions, skyrmionic phases can be found in the originally FM Pd/Co/Ir(111).

Here, we first perform a first-principles investigation of the electronic structure and magnetic properties of Pd/Fe and Pd/Co bilayers on an Ir(111) substrate. The analysis is focused on the conditions that lead to the emergence of noncollinear spin textures in Pd/Fe/Ir(111), in particular, skyrmionic phases (SkPs): In this paper, we consider a SkP the metastable state which presents skyrmions, which can be mixed with other magnetic structures (e.g., spin spirals) or not. Last, we explore, through atomistic spin-dynamics simulations, how the exchange interactions in the pristine Pd/Co/Ir(111) would have to be altered in order to support the creation of such SkPs, showing the resulting phase diagrams.

II. COMPUTATIONAL DETAILS

The electronic structure calculations were performed in the framework of the density functional theory (DFT) using the self-consistent real-space linear muffin-tin orbital method within the atomic sphere approximation (RS-LMTO-ASA) [40,41], which has been generalized to describe noncollinear magnetism [4,9,42–44].

The RS-LMTO-ASA is based on the LMTO-ASA formalism [45] and solves the eigenvalue problem directly in real space using the recursion method [46]. All calculations were performed within the local spin density approximation (LSDA) [47] and including SOC, $\vec{l}\cdot\vec{s}$, in each variational step [45]. In the recursion method, the continued fractions have been terminated with the Beer-Pettifor approach [48] after $LL = 22$ recursion levels. After the self-consistent procedure for the collinear solution, the isotropic exchange parameters J_{ij} are calculated with the Liechtenstein-Katsnelson-Antropov-Gubanov (LKAG) formula [49] as implemented in the RS-LMTO-ASA method [50,51], as well as the anisotropic exchange, DMI [52], $\vec{D}_{ij}$. We note that higher-order interactions (HOIs) can have an influence on the magnetic ordering. However, recent investigations [53] have shown that, for Co-based bilayers, the HOIs are relatively small; in the Pd/Fe/Ir(111) case, the four-spin interaction can lead to an enhancement of skyrmion stability.

For the calculated magnetic interactions here, we also considered both $J_{ij}(E)$, i.e., J_{ij} as a function of the integration energy limit (in the expression given in Ref. [49] for the exchange interactions), and the (s, p, d) orbital contributions to J_{ij} (calculated including only the corresponding orbital indices in the integration [50]). An analogous approach (replacing the integration limit to a given energy E) is here used to obtain the DMI vector components as a function of energy.

Pd/Fe and Pd/Co bilayers on Ir(111) substrates were simulated in real space by semi-infinite clusters with ∼16 000 atoms generated using the *fcc* Ir experimental lattice constant ($a = 3.84$ Å [54]). One layer of empty spheres was also included to simulate the vacuum region above the Pd layer. In all cases, the magnetic Fe (or Co) atoms are placed on the surface in the fcc stacking. Relaxations towards the surface in the real-space calculations were neglected, since our results presented already a good agreement with experimental observations [12,32].

After the electronic structure calculations, atomistic spin-dynamics (ASD) simulations were performed using the UPPASD package [55,56]. Using the *ab initio* calculated J_{ij} and $\vec{D}_{ij}$, the spin Hamiltonian $\mathcal{H}_i$ at a given site i can be obtained from

$$\mathcal{H}_i = -\sum_{i\neq j} J_{ij}(\hat{e}_i\cdot\hat{e}_j) - \sum_{i\neq j}\vec{D}_{ij}\cdot(\hat{e}_i\times\hat{e}_j) - \mu_B\sum_i \vec{B}\cdot\hat{e}_i + \sum_i K^i_{\text{eff}}(\hat{e}_i\cdot\hat{e}_z)^2, \tag{1}$$

where $\vec{B}$ is the external applied magnetic field (optionally included in the Hamiltonian), $\hat{e}_i$ is the direction of the local ith magnetic moment, μ_B is the Bohr magneton, and K^i_{eff} are the anisotropy strengths in the $\hat{e}_z$ direction (where $K^i_{\text{eff}} < 0$ indicates an out-of-plane easy axis). From this spin Hamiltonian, $\mathcal{B}^{\text{eff}}_i = -\frac{\partial\mathcal{H}_i}{\partial\hat{e}_i}$ of the Landau-Lifshitz-Gilbert (LLG) equation [56] can be obtained, which is then used in the ASD simulations.

In the ultrathin films investigated here, the dipole-dipole interaction energy term is small (of the order of 10^{-1} meV/atom) when compared with the DMI, and its effects can be reproduced by considering it as part of an effective anisotropy [57,58]. Therefore the K^i_{eff} parameters were split into two parts: (i) the SOC-induced magnetocrystalline anisotropy K^i_{SOC} and (ii) the so-called shape anisotropy K^i_{dd}, related to the dipole-dipole interactions. The K^i_{dd} values can be obtained by the Ewald summation technique [59]. In turn, K^i_{SOC} was obtained using the QUANTUM ESPRESSO (QE) package [60,61], using a fully relativistic scheme based on ultrasoft pseudopotentials [62]. In these QE calculations, the plane-wave basis set was considered within a cutoff of 110 Ry, and the Brillouin zones were sampled by a 12×12×2 $\vec{k}$-point mesh, following the Monkhorst-Pack method [63]. The Pd/Co/Ir(111) system was modeled with eight Ir layers and ∼10 Å of vacuum, while the first three layers were relaxed to achieve the optimal geometry. For Pd/Fe/Ir(111), we used the experimental value for the effective anisotropy of 0.4 meV/Fe [25,26].

The simulation of spin systems with the Hamiltonian given by Eq. (1) and subjected to periodic boundary conditions can exhibit an energy penalty if the cells are incommensurate with the magnetic textures. Here, we found that a square lattice with 250×250 atomic spins is suitable for simulating the Fe and Co layers of Pd/Fe/Ir(111) and Pd/Co/Ir(111). The convergence to an optimum state with ASD followed the simulated annealing (SA) method [64], gradually decreasing the temperature and equilibrating the spin configuration with the heat-bath Monte Carlo algorithm in every temperature step. Each simulation was performed two times, starting from a FM spin configuration and from a random (paramagnetic) spin configuration. The two total energies obtained from the SA were then compared, finally allowing the choice of the lower-energy state. For the Pd/Fe/Ir(111) phase diagram, we also started from the lowest-energy magnetic configuration in each point [30]. The presence of skyrmionic structures was analyzed through the topological charges Q of the entire spin lattice [65].

III. RESULTS

A. Magnetic moments and anisotropy

First, we performed calculations in a collinear approach for Pd/Fe and Pd/Co bilayers on Ir(111). The obtained spin magnetic moment m_s was 2.78 μ_B/atom at the Fe sites in Pd/Fe/Ir(111) and 1.85 μ_B/atom at the Co sites in Pd/Co/Ir(111). The Fe (Co) atoms induced spin polarizations on Pd sites at the outermost layer, and the magnetizations were not small: $m_s = 0.32$ μ_B/atom (0.30 μ_B/atom). On the other hand, the induced spin moments on Ir atoms in the first layer (denoted herein by Ir$_1$), nearest to the Fe (or Co) layer, -0.03 μ_B/atom, are small. The $-$ (+) sign indicates that the induced moments at Ir sites are aligned antiparallel (parallel) to the spin moments of the 3d metals. These Ir m_s quickly vanish with increasing distance from the magnetic layer, in a Friedel-like oscillatory pattern (such as the charge density). The orbital contributions to the magnetic moments (m_o) were all found to be relatively small: $m_o \sim 0.1$ μ_B/atom ($m_o \sim 0.09$ μ_B/atom) for Fe (Co), and $m_o \sim 0.03$ μ_B/atom for Pd. All magnetic moments obtained here are in agreement with previous results [31,32,66]. With these *ab initio* magnetic moments, the calculated K^i_{dd} parameter [see Eq. (1)] for the fcc(111) monolayer of Co is $K^i_{dd} = 0.16$ meV/atom, with an in-plane contribution, as expected. In turn, using the K^i_{dd} and the obtained $K^i_{\rm SOC}$ values from $\vec{k}$-space calculations, we find that the effective anisotropy strength [see Eq. (1)] is $K^i_{\rm eff} = -0.38$ meV/atom for Pd/Co/Ir(111). This $K^i_{\rm eff}$ was used in all spin-dynamics simulations reported later.

The spin-polarized local densities of states (LDOSs) for the d orbitals of representative layers among the systems studied here are shown in Fig. 1; s and p orbitals are not shown since they are very small. One can notice the similarity of the Fe [Fig. 1(a)] and Co [Fig. 1(b)] systems, where an almost rigid band model can be applied (roughly, it is the Fermi-level position, which is changed by adding one electron when going from Fe to Co). There is a relevant overlap energy interval of the 3d, 4d, and 5d states. Due to this large 3d-4d hybridization and the high Pd polarizability [66], there is an electron charge transfer from Pd 4d minority states to Fe 3d majority states, which explains the calculated non-negligible induced magnetic moment at the Pd surface layer. The Ir$_1$ LDOSs are more extended than the 3d and 4d elements.

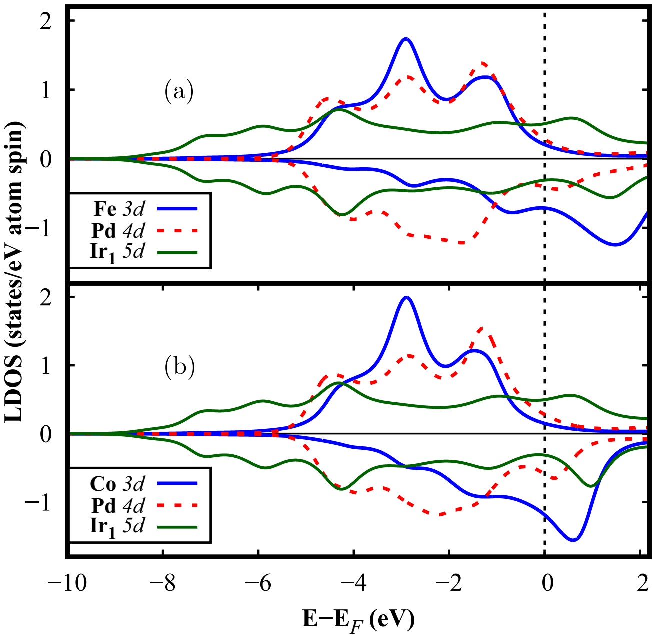

FIG. 1. Spin-polarized d-orbital projected local density of states (LDOS) in the Pd, the Fe, and the first Ir layer (Ir$_1$) in (a) Pd/Fe/Ir(111) and (b) Pd/Co/Ir(111). The minority densities of states are shown as negative.

B. Heisenberg exchange interactions

The calculations of the Heisenberg (isotropic), J_{ij}, and the DMI (anisotropic) exchange parameters were done for a collinear spin configuration, and we here consider an approximation [67] in which the Pd and Ir moments are treated as independent spin degrees of freedom. Figure 2 shows the intralayer 3d-3d, as well as the interlayer 3d-4d and 3d-5d J_{ij} parameters in Pd/X/Ir(111) (X = Fe, Co), including a comparison with Fe and Co fcc bulk exchange couplings, both with the same lattice parameter as Ir bulk.

Concerning the Pd/Fe bilayer on Ir(111), the intralayer isotropic exchange coupling $J_{\text{Fe-Fe}}$ is FM between spin moments of first-neighbor Fe atoms ($J^{\rm 1st}_{\text{Fe-Fe}} = 11.3$ meV), and its strength decreases with interatomic distance, oscillating between positive and negative values for more distant atoms. In particular, from the second neighbors to the fifth neighbors,

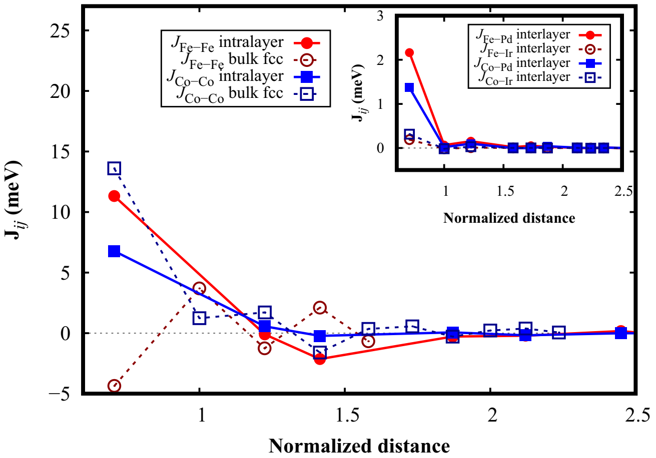

FIG. 2. Isotropic exchange coupling parameter J_{ij} between a 3d atom and a 3d atom as a function of the normalized interatomic distance (in units of the lattice parameter), for Pd/Fe/Ir(111) (solid red circles), Pd/Co/Ir(111) (solid blue squares), and the corresponding fcc bulks of Fe (dark red open circles) and Co (dark blue open squares). Data for fcc Co and fcc Fe were extracted from Refs. [50] and [71], respectively. Inset: exchange coupling between a 3d atom and a 4d atom and between a 3d atom and a 5d atom (interlayer) in Pd/Fe/Ir(111) (solid red circles and dark red open circles) and Pd/Co/Ir(111) (solid blue squares and dark blue open squares). The lines are guides for the eye.

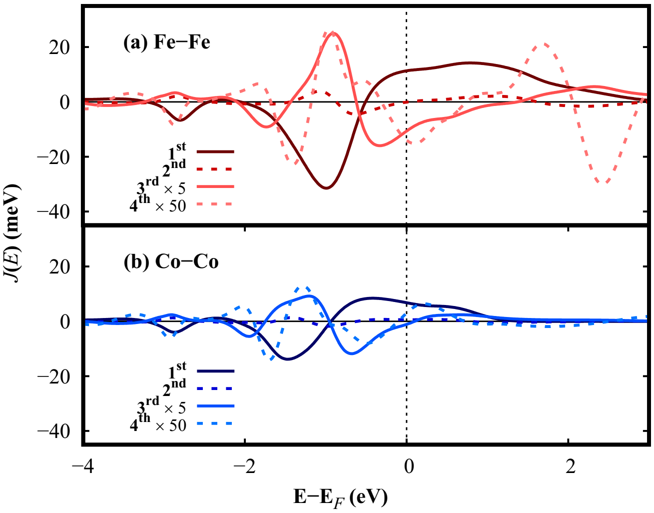

FIG. 3. Isotropic exchange coupling as a function of energy, J(E), between (a) Fe and (b) Co first-, second-, third-, and fourth-nearest neighbors for Pd/Fe/Ir(111) and Pd/Co/Ir(111). E_F is the Fermi energy.

the interactions favor the antiferromagnetic (AFM) coupling (with emphasis on the third-neighbor interactions, of $J^{3\mathrm{rd}}_{\text{Fe-Fe}} = -2.1$ meV), as shown in Fig. 2, which characterizes a long-range magnetic frustration effect. This remark is particularly relevant, given that frustrated isotropic exchange interactions have been shown to play a key role in the stabilization of complex noncollinear (spin-spiral, skyrmionic) states in transition metal two-dimensional (2D) systems [22,23], as well as that effective J_{ij}'s are closely related to the formation of lower-energy spin-spiral states [68]. Fe bulk fcc (γ-Fe) is known to exhibit a ground-state noncollinear magnetic ordering, very sensible to the lattice parameter [69], but the fcc structure is not the only cause [70] for the Fe noncollinearity in Pd/Fe/Ir(111): The $J^{1\mathrm{st}}_{\text{Fe-Fe}}$ is drastically modified when Fe changes from the fcc bulk structure to a monolayer (see Fig. 2). Beyond $\sim 2a$, the coupling $J_{\text{Fe-Fe}}$ becomes very small. These values are in agreement with earlier results for a Pd/Fe bilayer on Ir(111) [28,30,31]. The coupling between a typical Fe atom and its first-neighbor Pd is FM, to be precise, $J^{1\mathrm{st}}_{\text{Fe-Pd}} = 2.2$ meV, while the coupling between Fe and Ir nearest neighbors is much weaker (∼9% of the Fe-Pd interaction), as shown in the inset in Fig. 2, due to the large Ir bandwidth.

For Pd/Co/Ir(111), the intralayer isotropic exchange interaction is FM between Co first neighbors ($J^{1\mathrm{st}}_{\text{Co-Co}} = 6.8$ meV) and monotonically decreases to zero as the Co-Co distance increases. The third- and fifth-neighbor interactions favor the AFM coupling ($J^{3\mathrm{rd}}_{\text{Co-Co}} \approx J^{5\mathrm{th}}_{\text{Co-Co}} = -0.2$ meV), but the FM $J^{1\mathrm{st}}_{\text{Co-Co}}$ is the most relevant contribution. Therefore, unlike Pd/Fe/Ir(111) and even Co bulk fcc (see Fig. 2), no relevant AFM-FM competition is obtained for Pd/Co/Ir(111). The interlayer isotropic coupling between first-neighbor Co and Pd atoms is FM, $J^{1\mathrm{st}}_{\text{Co-Pd}} = 1.4$ meV. In order to analyze the isotropic exchange coupling behavior in more detail for Pd/Fe and Pd/Co on Ir(111), we show in Fig. 3 the J_{ij} as a function of energy between two Fe (or two Co) atoms, from first- up to fourth-nearest neighbors [$J_{\text{Fe-Fe}}(E)$ and $J_{\text{Co-Co}}(E)$]. The actual J_{ij} value (as expressed in Fig. 2) is obtained when $J(E)$ is at the Fermi level [$J(E = E_F)$]. From the inspection of the $J(E)$ curves around the Fermi level it can be inferred how structural relaxations as well as effects of increasing or reducing the band filling would affect the values of the isotropic exchange coupling parameter J_{ij} [9].

From Figs. 3(a) and 3(b), we can see that the nearest-neighbor coupling is by far the most important one. The similarity observed between the curves up to and near E_F for Fe-Fe and Co-Co exchange couplings suggests that we can assume a rigid-band-like model to explain the obtained difference between the $J_{\text{Fe-Fe}}$ and $J_{\text{Co-Co}}$ characters, attributing it to the extra 3d valence electron of Co when compared with Fe. With the displacement of the Fermi level in the Fe → Co transition, for instance, third neighbors' J_{ij}'s diminish in relative AFM strength, and fourth neighbors' exchange interactions change from AFM to FM in Pd/Co/Ir(111) [Fig. 3(b)]. As $J_{ij}(E)$ is modulated by the magnetic moment, $J_{\text{Co-Co}}$ curves are flatter than those of $J_{\text{Fe-Fe}}$.

Figure 3(a) shows that it is quite difficult to switch the interaction between Fe nearest neighbors from FM to AFM just by changing the band filling, since the $J^{1\mathrm{st}}_{\text{Fe-Fe}}(E)$ curve has a constant positive level around the E_F. Moreover, as also pointed out in Ref. [9], the structural relaxation would tend to shift the $J(E)$ curve to the right (higher values of energy). Thus this indicates that the FM coupling for this system will be, in general, stable under structural relaxations. In turn, Fig. 3(b) shows a qualitatively similar behavior for the interaction between Co nearest neighbors by changing the band filling, but with a decreasing $J^{1\mathrm{st}}_{\text{Co-Co}}(E)$ curve around E_F. For both systems, the exchange couplings between more distant Fe (or Co) neighbors are small.

Concerning the orbital projected contributions to the total $J_{\text{Fe-Fe}}$ and $J_{\text{Co-Co}}$ interactions [71], we first point out that s and p contributions are very small (always less than 2%) and therefore negligible. For both first- and fourth-neighbor interactions in the Pd/Fe and Pd/Co bilayers, the main contributions are from $3d_{xz}$-$3d_{xz}$ and $3d_{xy}$-$3d_{xz}$ orbitals. For second- and third-neighbor interactions, however, it is interesting to notice that the shift in E_F changes the major orbital projected contributions. Regarding the second-neighbor interactions, the main contributions for the total J_{ij}'s in Pd/Fe/Ir(111) and Pd/Co/Ir(111) come from $3d_{xy}$-$3d_{z^2}$ and from $3d_{xy}$-$3d_{xy}$, $3d_{z^2}$-$3d_{z^2}$, and $3d_{xz}$-$3d_{xz}$, respectively. In turn, for third neighbors, the main contributions arise from $3d_{xz}$-$3d_{xy}$, $3d_{xz}$-$3d_{xz}$, and $3d_{xz}$-$3d_{z^2}$ for Pd/Fe/Ir(111) and from $3d_{xz}$-$3d_{z^2}$ for Pd/Co/Ir(111). These changes in second- and third-neighbor J_{ij} interactions are important and will be explored in Sec. III D when analyzing the boundaries for the emergence of noncollinear textures in Pd/Fe/Ir(111).

C. Dzyaloshinskii-Moriya interactions

Turning now to the anisotropic DMI, we first stress that this interaction comes as a surface effect. Let us consider the interaction vector $\vec{D}_{ij} = (D_x, D_y, D_z)$ between i and j sites ($i \neq j$), whose components are individually denoted by D_ν ($\nu = \{x, y, z\}$). Herein, the z axis is considered to be out of plane ($z \parallel [\bar{1}\bar{1}\bar{1}]$), and (D_x, D_y) are in-plane components, where the x axis is parallel to the nearest Fe-Fe (or Co-Co) bond

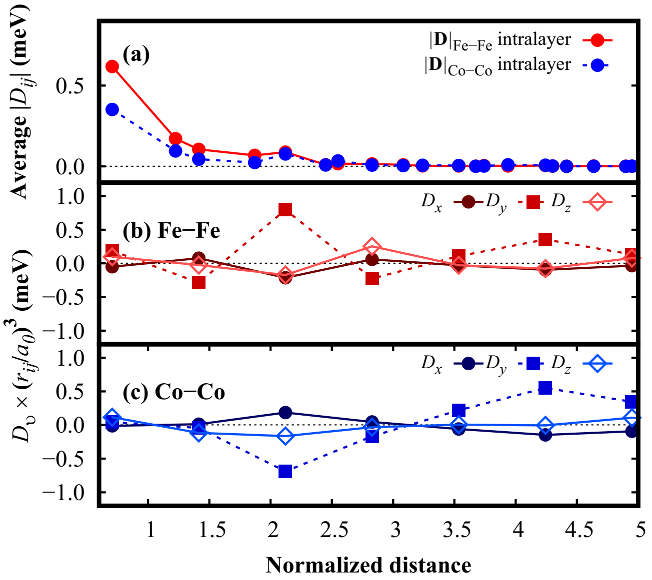

FIG. 4. Average magnitude of (a) the DMI vectors, $|\vec{D}_{ij}|$, for *all* possible Fe-Fe (or Co-Co) bonds in an fcc(111) layer, and (b) and (c) D_x, D_y, and D_z components times $(\frac{r_{ij}}{a})^3$, as a function of the normalized interatomic separation (in units of the lattice parameter) for Fe-Fe (b) and Co-Co (c) atoms, considering *only* the in-plane $[\bar{1}01]$ pairing direction. The DMI calculations were performed with a collinear magnetic configuration. The lines are guides for the eye.

direction. Figure 4 shows the average magnitudes of $\vec{D}_{ij}$ between the two Fe (two Co) atoms as a function of the interatomic distance for Pd/Fe/Ir(111) [Pd/Co/Ir(111)], as well as the components, considering the in-plane $[\bar{1}01]$ pairing direction. It can be seen from Fig. 4(a) that, in both cases, the magnitude of the DMI vector between two Fe (or two Co) atoms is larger for the first neighbors (D^{1st}). Moreover, the magnitude of the DMI vector tends to decrease with respect to the interatomic separation, but not monotonically, presenting peaks for enlarged pairwise distances, such as $\frac{3}{2}\sqrt{2}a$ (~8.2 Å). This demonstrates the long-range nature of the DMI in these systems, as a consequence of electronic hopping mediated mostly by the extended Ir $5d$ states (Fig. 1). We obtained $D^{\text{1st}}_{\text{Fe-Fe}} = 0.62$ meV, for the Fe nearest-neighboring interactions, which reveals a good agreement with previous studies ($D^{\text{1st}}_{\text{Fe-Fe}} = 0.82$ meV for a 5% inward relaxed Fe layer [28], and $D^{\text{1st}}_{\text{Fe-Fe}} = 1.00$ meV for the pristine Pd/Fe/Ir(111) system [31]), considering the different theoretical approaches used. Given the simple FM (single domain) observed for Pd/Co/Ir(111) [32], it is relevant to notice also the relatively high $D^{\text{1st}}_{\text{Co-Co}}$ value of 0.35 meV. Concerning the DMI vector components, we notice that in both Pd/Fe/Ir(111) and Pd/Co/Ir(111) multilayers, all D_υ components between two Fe (or two Co) atoms exhibit an oscillatory character, especially D_y, as shown in Figs. 4(b) and 4(c), in a Ruderman-Kittel-Kasuya-Yosida-like (RKKY-like [72–74]) behavior [75], mediated by the conduction electrons [76]. These oscillations in D_υ cause the DMI to vary its orientation as the distance from the reference atom changes.

This can be directly seen in Fig. 5, where we present the DMI directions between a typical atom in the $3d$ monolayers and its intralayer neighbors and where the colors (arrows) denote, respectively, the modulus (orientation) of $\vec{D}_{ij}$, in the case of a collinear magnetic configuration calculation. For both Pd/Fe and Pd/Co bilayers on Ir(111), an inspection of Fig. 5 shows that the DMI directions keep the C_{3v} point-group symmetry of the fcc(111) layer, always following the relation $\vec{D}_{ij} \cdot \vec{r}_{ij} \sim 0$ ($\vec{r}_{ij} = \vec{r}_i - \vec{r}_j$ is the position vector), the only constraint for this type of surface expected from Moriya's symmetry rules [20,77]. A similar result was found in Ref. [28] for the Pd/Fe/Ir(111) system. In Fig. 5(a), it is worth noting that the average angle between the nearest-neighbor (NN) $\vec{D}_{\text{Fe-Fe}}$ and the Ir(111) surface plane, $\bar{\phi}$, is $\bar{\phi} \sim 26.5^\circ$. This mostly in-plane $\vec{D}^{\text{1st}}_{\text{Fe-Fe}}$ (the most prominent) favors a rotation of the local spin moments towards the Ir(111) surface to minimize the system energy, directly influencing the emergence of noncollinear magnetism. The reasoning is the same for $\vec{D}^{\text{2nd}}_{\text{Fe-Fe}}$ and $\vec{D}^{\text{3rd}}_{\text{Fe-Fe}}$, especially because of the long-range influence of D_y [see Fig. 4(b)]. Concerning the $\vec{D}_{\text{Co-Co}}$ interaction vectors, from Fig. 5(b), almost out-of-plane nearest-neighbor DMI vectors are shown. Indeed, the obtained average angle between the $\vec{D}^{\text{1st}}_{\text{Co-Co}}$ and the Ir(111) surface is about $\bar{\phi} \sim 68.6^\circ$. When moving to further neighborhoods, and following the long-range D_y RKKY-like influence [Fig. 4(c)], $\vec{D}_{\text{Co-Co}}$ periodically changes from almost in plane to almost out of plane. Therefore an opposite behavior of $\vec{D}^{\text{1st}}_{\text{Co-Co}}$ is verified when comparing Pd/Fe/Ir(111) and Pd/Co/Ir(111) systems. It is also worth stressing that the chirality is changed for second-neighbor DMI, but maintained for nearest-neighbor $\vec{D}_{ij}$.

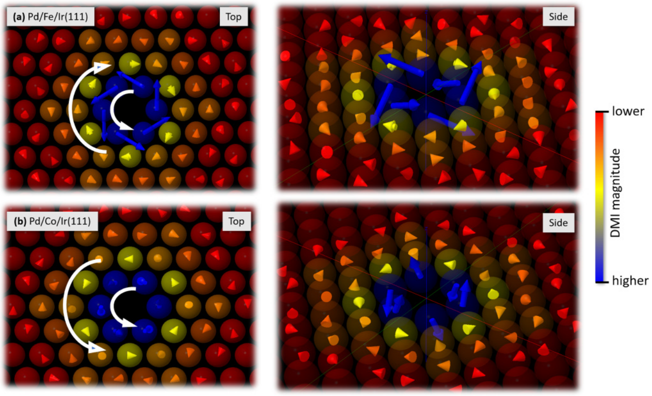

FIG. 5. Schematic top and side views of a typical $3d$ atom (in dark gray) and its closer neighbors in (a) Pd/Fe and (b) Pd/Co bilayers on Ir(111) surfaces. The arrows indicate the DMI vectors between the central atom and the atom in which the arrow is located, while the DMI magnitude is represented by the color scheme (as indicated in the color bar). The z axis corresponds to the out-of-plane direction ($[\bar{1}\bar{1}\bar{1}]$).

An analogous investigation to that done for J_{ij} in Fig. 3 can be done for the DMI. Let us consider $\vec{D}_{ij}(E)$ the interaction vector as a function of the energy for each component, $D_\upsilon(E)$. The results for Fe-Fe and Co-Co interactions for the in-plane pairing direction $[\bar{1}01]$ are shown in the left and right panels of Fig. 6, respectively. The results are similar for the $[\bar{1}10]$ in-plane direction (data not shown). For $\vec{D}_{ij}(E)$ we also obtain very similar curves for the Fe-Fe and Co-Co cases, indicating,

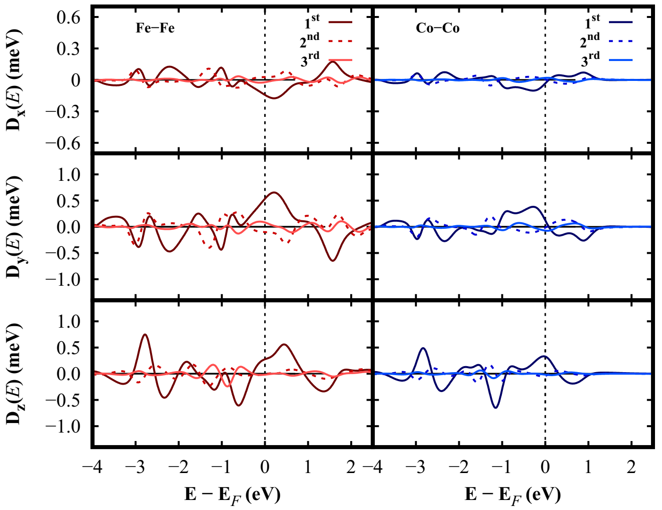

FIG. 6. Anisotropic DMI vector components D_x, D_y, and D_z as a function of the energy, between Fe (left panels, red curves) and Co (right panels, blue curves) first-, second-, and third-nearest neighbors for the Pd/Fe/Ir(111) and Pd/Co/Ir(111) in the in-plane $[\bar{1}01]$ pairing direction. E_F is the Fermi energy.

again, that a simple rigid-band-like model can be used to explain the differences in the DMI directions in both systems. The extra $3d$ valence electron in the minority spin states of Co shifts E_F to higher energies, in a region in which D_z is more pronounced in Pd/Co/Ir(111), diminishing at the same time the corresponding importance of the D_x and D_y components. In Pd/Fe/Ir(111), however, the case is the inverse: While $D_z(E_F)$ becomes relatively smaller, $D_x(E_F)$ and $D_y(E_F)$ become comparatively relevant, constraining $\vec{D}_{ij}$ to a more in-plane interaction vector ($\vec{D}_{ij} \perp [111]$). Even though the $D_\nu(E)$ curve profiles for Pd/X/Ir(111) (X = Fe, Co) are very similar to each other, their magnitudes differ (being smaller for Co-Co interactions), a trend which is indirectly driven by Hund's first rule [78]. With this simple rigid-band-like model, for example, it is also possible to predict the situation of one $3d$ valence electron *more* in Co (Co → Ni), in which E_F is shifted to higher energies. The DMI would diminish in magnitude, especially due to the lower peaks in $D_\nu(E)$ (in accordance with Ref. [78]), and the interaction vectors would be prominently in plane [79] (while J_{ij} would present FM neighbor couplings; see Fig. 3(b) and Ref. [79]). The analysis of D_z on Pd/Fe/Ir(111) and Pd/Co/Ir(111) also suggests that the DMI would not be profoundly affected by small structural relaxations.

In order to compare our results for the DMI with the experimental one concerning the Pd/Fe/Ir(111) [25], which obtained $D = (3.9 \pm 0.2)$ mJ/m^2, expressed as an energy density [80], one can define an effective DMI vector magnitude as $D^{\text{eff}} = \sum_{i \neq 1} |\vec{D}_{1i}|$, where site "1" represents a reference (Fe or Co) site (central atom) and the sum goes over its nearest-neighbor atoms of the $3d$ intralayer hexagon, presenting an area of $\frac{3l^2\sqrt{3}}{2}$, with $l = a\frac{\sqrt{2}}{2}$. Therefore our first-principles DMI vector density D for the Fe layer in Pd/Fe/Ir(111) is equal to $D = D_{\text{Fe}} = \frac{D^{\text{eff}}}{\frac{3l^2\sqrt{3}}{2}} = \frac{3.72\ \text{meV}}{19.16\ \text{Å}^2} \sim 3.1$ mJ/m^2, which is in good agreement with the experimental result. For Pd/Co/Ir(111) this quantity is ~60% of D_{Fe} ($D_{\text{Co}} \sim 1.8$ mJ/m^2).

TABLE I. First-principles damping values calculated for a typical atom in the Fe (α_{Fe}), Co (α_{Co}), and Pd (α_{Pd}) layers of Pd/Fe/Ir(111) and Pd/Co/Ir(111).

Pd/Fe/Ir(111)	Pd/Co/Ir(111)
$\alpha_{\text{Fe}} = 0.004$ [85]	$\alpha_{\text{Co}} = 0.003$ [85]
$\alpha_{\text{Pd}} = 0.192$	$\alpha_{\text{Pd}} = 0.274$

Skyrmion formation and shape are often related to the ratio between the anisotropic and the isotropic exchange couplings [14,28,81,82]. For the Pd/Fe/Ir(111) system, we obtained $\frac{|\vec{D}|}{J} \sim 0.055$ for the average nearest-neighbor Fe-Fe interactions, which is in agreement with Ref. [28]. Interestingly, for the Pd/Co/Ir(111) this value is similar, $\frac{|\vec{D}|}{J} \sim 0.051$. As skyrmions in Pd/Fe/Ir(111) were experimentally verified [12], one would have expected, by looking at the higher $\frac{|\vec{D}|}{J}$ obtained ratio, that Pd/Co/Ir(111) has a tendency towards the emergence of noncollinear spin configurations or even skyrmions. Nevertheless, this is not the case [32].

D. Phase diagrams and boundaries for the noncollinear textures

So far, we have shown that a simple rigid-band-like model can explain the differences in the *ab initio* J_{ij} and $\vec{D}_{ij}$ parameters of Pd/Fe and Pd/Co bilayers on Ir(111). Also, we have demonstrated the long-range character of $\vec{D}_{ij}$ and the in-plane (or out-of-plane) preference of the DMI vectors. Now, we apply these parameters that we have obtained in the DFT calculations in the ASD simulations, constructing the magnetic configurations for several external magnetic field B and temperature T conditions. Before we discuss our results, however, it is noteworthy that we had to consider not only the first shell of Fe-Fe and Co-Co neighbors in the simulations, but also further neighbors to obtain the correct magnetic configurations for Pd/Fe/Ir(111) and Pd/Co/Ir(111), as will be discussed later in this section. Concerning Pd/Fe/Ir(111), it was experimentally [12,25,83] and theoretically [27,28,30,31,84] shown that the system presents a spin-spiral (SS) ground state which evolves into a FM skyrmion lattice (SkL) when an external magnetic field is applied (of ~1–1.5 T), reaching a FM (field-polarized) state for $B \sim 2.5$–3 T. However, Pd/Co/Ir(111) presents a single-domain FM state in an applied field of $B = \pm 1$ T [32]. We explored the ground and excited states (with $B > 0$ and $T > 0$) of both systems, for external magnetic fields applied in the out-of-plane direction. In all simulations we considered the *ab initio* Gilbert damping values of $\alpha_{\text{PdFe}} = 0.023$ for Pd/Fe/Ir(111) and $\alpha_{\text{PdCo}} = 0.040$ for Pd/Co/Ir(111), obtained with the same method for calculating α in real space as described in Ref. [85]. These α values take into account the moment-weighted average of the layer-resolved dampings shown in Table I for typical sites in the Fe (or Co) layers [85] and typical sites in the corresponding Pd layers. For example, $\alpha_{\text{PdCo}} = \frac{m_s^{\text{Pd}}\alpha_{\text{Pd}} + m_s^{\text{Co}}\alpha_{\text{Co}}}{m_s^{\text{Pd}} + m_s^{\text{Co}}}$. The results presented here are not strictly dependent on the damping parameter choice. We note, however, that one should be careful when using the damping values for the investigation

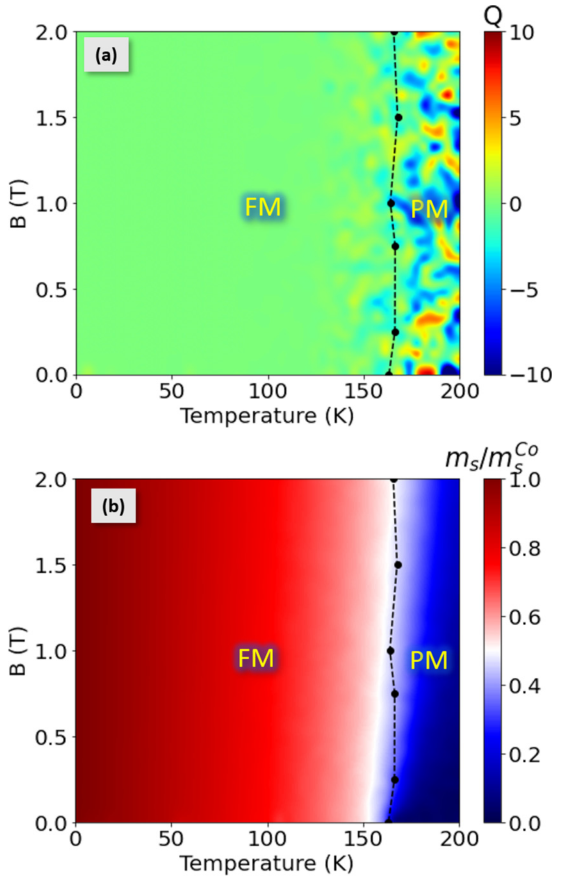

FIG. 7. *B-T* phase diagram of Pd/Co/Ir(111), showing (a) the time-average total topological number $\bar{Q}$ and (b) the average relative magnetic moment ($\frac{\bar{m}_s}{m_s^{\text{Co}}}$) as a function of external *B* and finite *T*. The black dots show the order transition inflection points of the magnetic specific heat, c_V, obtained by a Lorentzian fitting. The ferromagnetic (fully saturated, FM) and paramagnetic (PM) phases are indicated. The dashed black lines are guides for the eye.

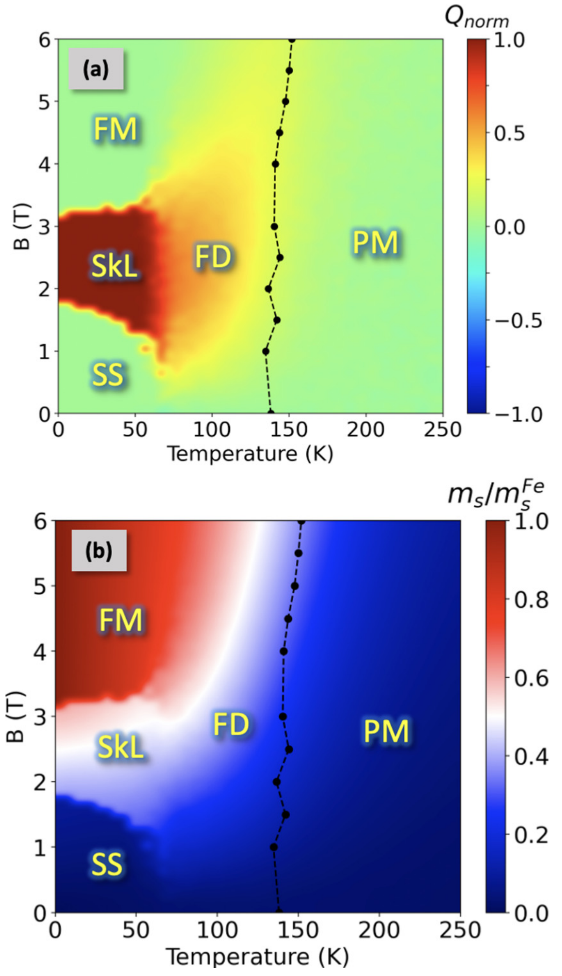

FIG. 8. (a) and (b) The same as Fig. 7, but for Pd/Fe/Ir(111) with the normalized topological charge Q_{norm}. The ferromagnetic (fully saturated, FM), spin-spiral (SS), skyrmion lattice (SkL), fluctuation-disordered (FD), and paramagnetic (PM) phases are indicated in yellow. The dashed black lines are guides for the eye.

of α-dependent properties, as the effective α has been shown to change when in noncollinear spin environments [such as in Pd/Fe/Ir(111)] [86,87].

The obtained (B, T) phase diagram of Pd/Co/Ir(111), based on the time average (1 ps) of the topological charge Q, is exhibited in Fig. 7(a). In the presence or in the absence of magnetic fields, the Co-based system presents a single-domain FM state. This is corroborated by the average magnetic moments $\bar{m}_s$ [Fig. 7(b)], in which the $\bar{m}_s$ value decays regularly with temperature as an effect of time-dependent fluctuations. From our *ab initio* and spin-dynamics calculations, the Pd/Co/Ir(111) FM phase was not modified to a noncollinear texture under the influence of an external magnetic field (evaluated in the in-plane and out-of-plane directions, for field magnitudes up to $B = 100$ T). The calculated critical temperature from the peak (divergence) in the magnetic specific heat [88], $c_V = \frac{\partial E}{\partial T}|_V$, is about $T_C \approx 165$ K (black dots in Fig. 7, obtained by a Lorentzian fitting). The calculated T_C is far below the Co fcc bulk limit, in qualitative agreement with Ref. [89]. For $T > T_C$, the random distribution of spin directions over *finite* spaces and times led to arbitrary noninteger Q values, characterizing the paramagnetic phase.

In turn, for Pd/Fe/Ir(111), we obtained a much more complex phase diagram, shown in Fig. 8. The most relevant is a SkL phase that occurs when $1.7\text{ T} \lesssim B \lesssim 3\text{ T}$, excluding an intermediate region, mainly composed by a mixed (SS + skyrmions) state, accessed by SA simulations. The skyrmions vary in diameter and density as the applied magnetic field increases. Our calculations show that, for instance, at $T \sim 0$ K the diameter changes from $d \sim 4.4$ nm for $B = 1.8$ T to $d \sim 3.9$ nm for $B = 3.3$ T, a reduction of $\sim$12% in the average value, in accordance with Refs. [25,90,91]; their shape, however, switches from the well-known circular shape to an amorphic shape due to thermal fluctuations for finite temperatures. Above $B \sim 3$ T, the skyrmions gradually vanish, leading to a FM state. Indeed, the skyrmion density is reduced from $\sim 68\times10^{-3}$ skyrmions/nm^2 for $B \sim 1.8$ T (skyrmion lattice) to $\sim 16\times10^{-3}$ skyrmions/nm^2 for $B \sim 3.3$ T. This transition is characterized by the presence of increasingly isolated skyrmions. Again using the criteria of divergence in c_V, the calculated T_C to the PM phase is about $T_C \approx 145$ K

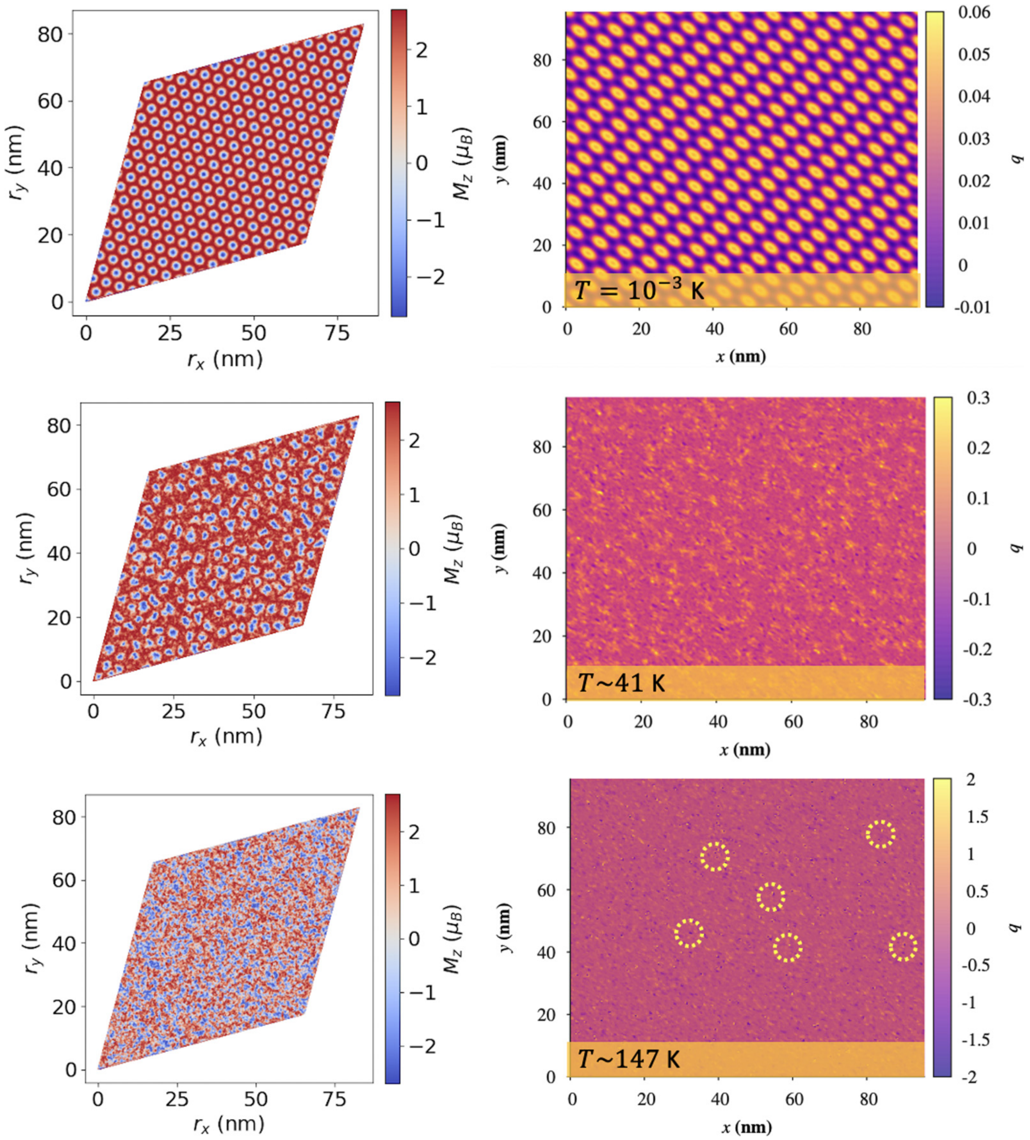

FIG. 9. Left column: Real-space image of spin configurations of Pd/Fe/Ir(111) for an applied external field of $B \sim 2.6$ T and temperatures of $T = 10^{-3}$ K, $T \sim 41$ K, and $T \sim 147$ K, with the local z component of the magnetic moment, m_z, indicated by the color bars (in μ_B). Right column: Corresponding topological charge densities with intensity given by the color bars. The yellow dotted circles indicate the occurrence of positive and negative poles for better visualization. Here, r_x and r_y are positions in real space (given in nanometers).

(see the black dots in Fig. 8). Differently from Pd/Co/Ir(111), the transition region to the PM phase is not characterized by an abrupt shift to arbitrary noninteger Q values, but instead by a zone composed by arbitrary *rational* topological charges with the same sign found for Q's in the SkL region; previous studies usually call it a fluctuation-disordered (FD) state [27,30,83], where the skyrmion lifetime is finite. In terms of the topological charge densities, states in the FD state are composed by short-lived (positive and negative) poles, as shown in Fig. 9 (for $T \sim 147$ K). In contrast, for finite temperatures inside the SkL region (Fig. 9, $T \sim 41$ K), the topological charge densities are composed of amorphic geometries indicating the positions where skyrmions are found in real space. The transition to the FD state, at about $T \sim 70$ K, agrees very well with recent experiments [83].

Below $B \sim 1.7$ T (or $B \sim 1$ T, including the intermediate region), we find a SS configuration with a wavelength of $\lambda \sim 4$ nm when $B = 0$ T, in excellent agreement with experimental results of $\lambda = 5$–7 nm [12,92]. This is also corroborated by the average magnetic moment investigation [see Fig. 8(b)], in which $\bar{m}_s \rightarrow 0$ for this range of B values. We note that because of the general FM character of Pd-Fe J_{ij} interactions (see inset in Fig. 2), induced by the high hybridization of the Fe-Pd ($3d$-$4d$) electronic states (Fig. 1), the Pd cover layer replicates the magnetic configuration formed in the Fe layer, however, with lower intensity (due to the diminished induced magnetic moment of Pd in comparison to Fe). This result was confirmed with atomistic spin-dynamics simulations (data not shown), and it is in agreement with the observations in Ref. [12], in which the Pd/Fe bilayer behaves as a single magnetic entity.

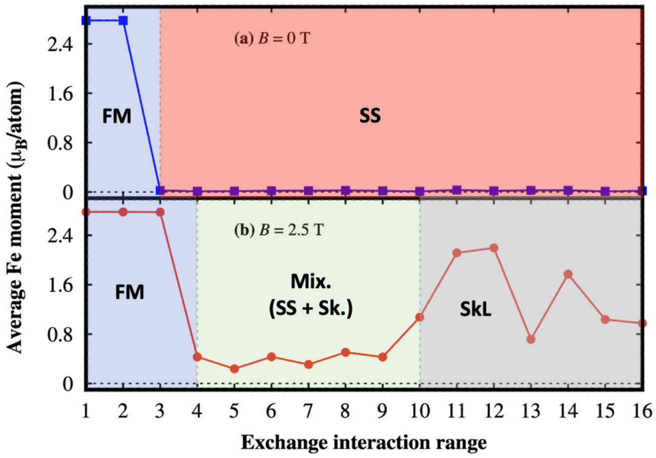

FIG. 10. Evolution of the average Fe m_s in Pd/Fe/Ir(111) at low temperature ($T = 10^{-3}$ K), for (a) $B = 0$ T and (b) $B = 2.5$ T, as further J_{ij} interactions are considered (e.g., "1" indicates up to first neighbors), and in the presence of DMI and the experimental anisotropy. Lines are guides for the eye. Mix., mixed; Sk., isolated skyrmionic structures.

1. *Boundaries for the noncollinear textures at low temperatures*

Having established the phase diagrams, natural questions that arise are as follows: Which interactions are essential to the emergence of noncollinear textures in Pd/Fe/Ir(111)? Does Pd/Co/Ir(111) ever present a noncollinear behavior for the consideration of distinct interaction neighborhoods? To answer these questions, we performed several low-temperature SA calculations with different ranges of J_{ij} and $\vec{D}_{ij}$ interactions, for both surfaces. In the case of Pd/Co/Ir(111), considering DMI and J_{ij}'s up to *fifth* neighbors and disregarding B and the anisotropy term, we found noncollinear configurations (SS, with $\lambda > 40$ nm, and SkL, composed by skyrmions with $d > 20$ nm) as almost degenerated lower-energy solutions. In contrast, when K^i_{eff} is included [Eq. (1)], we always find a FM (single-domain) solution as the most stable; therefore the shift of E_F to higher energies, turning second neighbors and further J_{ij} interactions to positive (or less negative) values, indeed vanishes the possibility of a noncollinear ordering in the Pd/Co bilayer.

For Pd/Fe/Ir(111), however, the case is more interesting. Without considering DMI, the inclusion of J_{ij}'s from fourth to seventh neighbors results in isolated skyrmionic structures as metastable solutions in the presence of external magnetic fields, alternating between stable SS, in agreement with Ref. [31], and mixed states when $B = 0$. With the full J_{ij} set and $(B, K^i_{\text{eff}}) = (0, 0)$, we find noncollinear metastable solutions (FM ground state [28]). In turn, in the presence of DMI, $B = 0$, and high anisotropies (~1 meV/Fe), the consideration until *third*-neighbor interactions produces chiral skyrmions with arbitrary topological charge [93] as metastable solutions. With the experimental anisotropy and the inclusion of J_{ij}'s further than third neighbors, we observe the main transition to the SS phase. When $B = 2.5$ T, the fourth-neighbor J_{ij}'s also produce a FM → mixed state (SS + skyrmions) transition, while the SkL (Fig. 8) only emerges when considering *tenth*-neighbor interactions. Figure 10 summarizes the regions for Pd/Fe/Ir(111) when DMI is present for different neighborhoods of exchange interactions. In brief, the fact that the first-neighbor DMI Fe-Fe interaction has a relevant in-plane component is a necessary although not a sufficient condition to drive the complex noncollinear configurations here.

E. Tuning Pd/Co/Ir(111)

Now, we explore the possibility of tuning the magnetic (J_{ij} and $\vec{D}_{ij}$) parameters of Pd/Co/Ir(111), aiming for the emergence of noncollinear textures in this material which has a simple (single-domain) magnetic configuration. As mentioned in the Introduction, recent investigations have shown that these intrinsic interactions can be experimentally modified by the application of external electric fields or strain or by introducing high-spin-orbit defects. Also, considering the demonstrated rigid-band-filling nature of the interactions, one can modify the J_{ij} and $\vec{D}_{ij}$ by shifting E_F through, for instance, FeCo alloying [26,94]. Therefore, in this section we consider initially the *ab initio* parameters calculated for Pd/Co/Ir(111), which, after being tuned, will be analyzed separately.

Since the DMI presents an essentially distinct behavior in Fe-based and Co-based bilayers, we inspect how the orientations and magnitudes influence the emergence of skyrmions. Figure 11 shows the absolute topological charge phase diagrams for the applied magnetic fields $B = 0.1$ T and $B = 0.5$ T as a function of the DMI vector rotations and magnitudes (exchange couplings are not changed). The $\vec{D}_{ij}$ orientations are varied from the ones obtained for Pd/Co/Ir(111) (0%) to the ones obtained for Pd/Fe/Ir(111) (100%), considering an interaction distance up to almost ~2.7 nm (35 shells of neighbors, or ~$7a$). Here, we generalize naming the set of these states as skyrmionic phases (SkPs). If Pd/Co/Ir(111) DMI is simply twisted, keeping its strength [white dashed line labeled "Co" in Figs. 11(a1) and 11(b1)], no noncollinear configuration is achieved. On the other hand, if the Co-Co DMI magnitude is increased, isolated skyrmionic structures (Sk) or mixed states (Sk + SS) are found in the rotation interval of ~15 to ~100%, for both analyzed magnetic fields; as B is enhanced, we also obtain an increase in the skyrmion counting in this region (higher Q's). An example state considering a rotation of ~50% of the DMI orientation of Pd/Fe/Ir(111) and double the original $\vec{D}_{\text{Co-Co}}$ magnitude, for $B = 0.1$ T, is shown in Fig. 12. The energy differences from the FM (single-domain) state as well as a comparison with the SS phase in the $\hat{x}$ and $\hat{y}$ directions ($1\mathbf{q}\,yz$ and $1\mathbf{q}\,xz$, respectively), and with a pure SkL phase ($3\mathbf{q}$), are calculated. As can be seen, both SS ($\Delta E \sim 14$ μeV/Co) and SkL ($\Delta E \sim 42$ μeV/Co) present small energy differences with respect to the FM configuration, thus being characterized by metastable solutions in the whole range of spin lattice sizes. The situation is similar to that reported for Co/Ru(0001) [18], in which metastable isolated skyrmions are found.

In Fig. 11, for DMI directions between ~40 and ~60% of $\vec{D}_{\text{Fe-Fe}}$, and $B = 0.1$ T, a mixed phase (SS + skyrmions) can occur especially near higher $\vec{D}_{ij}$ magnitudes (near two times $\vec{D}_{\text{Co-Co}}$). This region vanishes when higher external magnetic fields (such as $B = 0.5$ T) are applied, making room for an isolated-skyrmion phase. The situation is similar in the

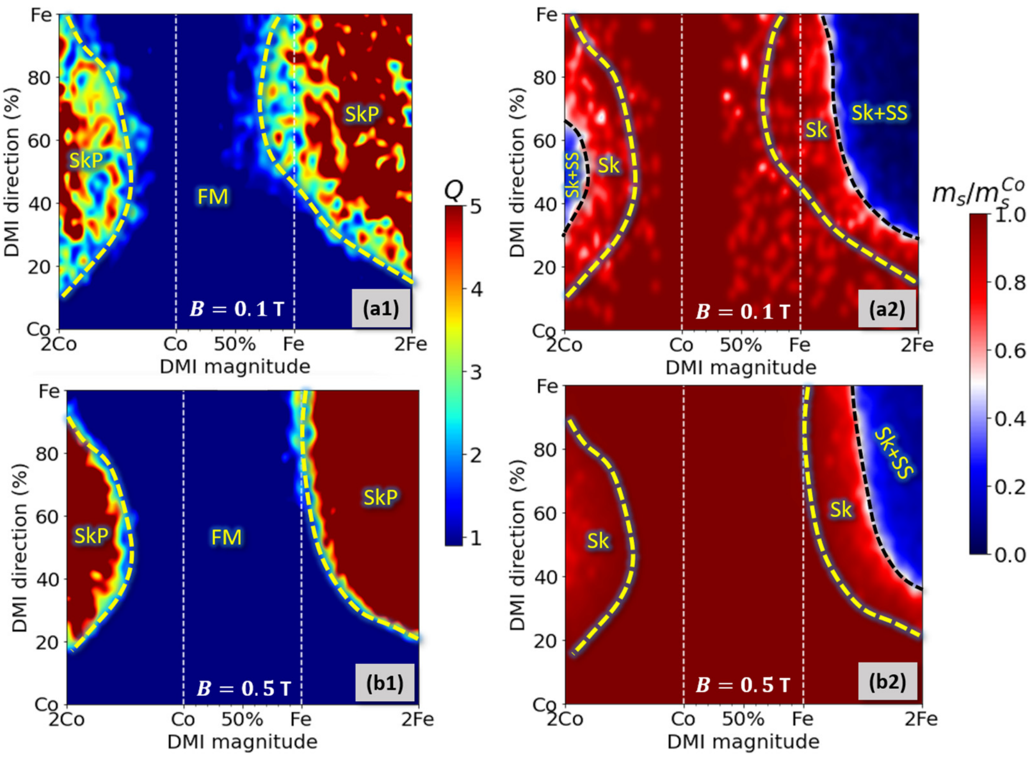

FIG. 11. Skyrmion phase diagrams and the corresponding average relative spin moments ($\frac{m_s}{m_s^{\text{Co}}}$) with respect to the applied magnetic fields of (a1) and (a2) $B = 0.1$ T and (b1) and (b2) $B = 0.5$ T, as a function of the DMI vector directions and magnitudes. Directions of 0 and 100% represent the original Pd/Co/Ir(111) and Pd/Fe/Ir(111) DMI orientations, respectively. The $\vec{D}_{ij}$ magnitude, ranging from two times the Pd/Co/Ir(111) DMI (2Co) to two times the Pd/Fe/Ir(111) DMI (2Fe), passes through an intermediate transition from $|\vec{D}_{\text{Co-Co}}|$ to $|\vec{D}_{\text{Fe-Fe}}|$. The absolute topological charges are indicated in the color bar, and the ferromagnetic (FM, single-domain), skyrmionic (SkP), isolated-skyrmion (Sk), and mixed (Sk + SS) phases are labeled. In all simulations, we considered $T = 10^{-3}$ K. The dashed white, yellow, and black lines are guides for the eye.

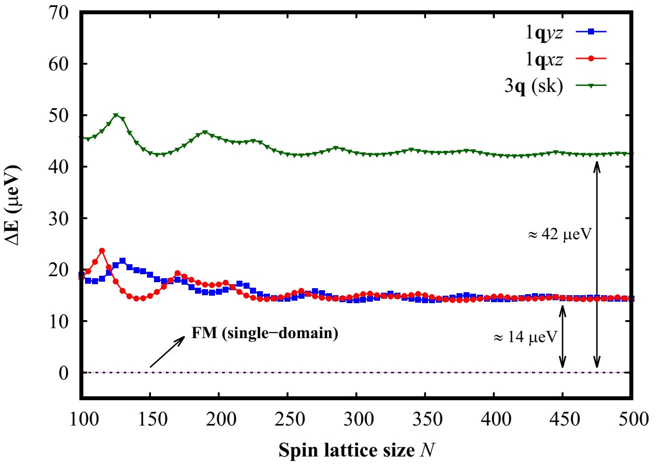

FIG. 12. Energy difference, ΔE, with respect to the FM single-domain configuration (dashed line) as a function of the spin lattice size N for the SS phase in the $\hat{y}$ ($1\mathbf{q}\,xz$, red dots) and $\hat{x}$ ($1\mathbf{q}\,yz$, blue squares) directions and for the SkL phase ($3\mathbf{q}$, green triangles). For the simulations, the J_{ij} interaction set is kept as the one obtained for Pd/Co/Ir(111). DMI magnitudes are two times the original $|\vec{D}_{\text{Co-Co}}|$ and rotated to ~50% of the Pd/Fe/Ir(111) $\vec{D}_{ij}$ directions. In all cases, we considered $T = 10^{-3}$ K and $B = 0.1$ T.

Co → Fe transition and higher DMI magnitudes, except that, even for $B = 0.5$ T, a region characterized by mixed states still survives. In this case, following the trends shown by Figs. 11(b1) and 11(b2), the large DMI magnitudes require even higher external fields to transform this (SS + Sk) region into an isolated-skyrmion zone.

The effect of exchange coupling frustrations is investigated in Fig. 13, which shows the skyrmion phase diagram as a function of the J_{ij} strength and the applied B; in this case, the original DMI magnitudes and directions of Pd/Co/Ir(111) are not modified. This transition allows for $J_{\text{Co-Co}}$ to transform into $J_{\text{Fe-Fe}}$ in an interaction distance up to ~2.7 nm (or ~7a), so the FM-AFM exchange coupling competition existing in Pd/Fe/Ir(111) gradually emerges. Interestingly, we note that a SkP only appears near the $J_{\text{Fe-Fe}}$ line [white dashed line labeled "Fe" in Figs. 13(a) and 13(b)], for external magnetic fields smaller than $B = 2.5$ T. At J_{ij} strengths higher than $J_{\text{Fe-Fe}}$, the strong frustration induced forces the system into a metastable isolated-skyrmion phase, especially for low external magnetic fields. Therefore the effect of magnetic frustration is sufficient to render skyrmions from about the $J_{\text{Fe-Fe}}$ limit, which are stabilized with the help of magnetic fields, the not completely out-of-plane $\vec{D}_{\text{Co-Co}}$, and an out-of-plane magnetic anisotropy. The latter has been previously

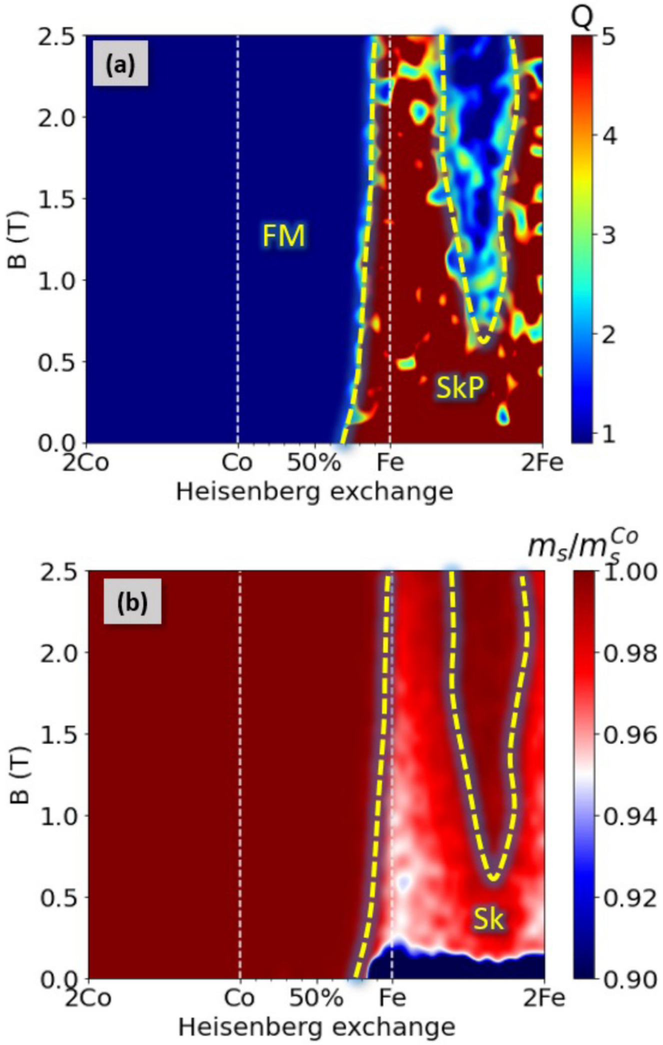

FIG. 13. (a) Skyrmion phase diagram and (b) the corresponding average relative spin moments ($\frac{m_s}{m_s^{\text{Co}}}$) as a function of the exchange coupling J_{ij} and external magnetic field B. The exchange magnitudes are varied from two times the Pd/Co/Ir(111) J_{ij}'s (2Co) to two times the Pd/Fe/Ir(111) J_{ij}'s (2Fe), passing through an intermediate transition from $J_{\text{Co-Co}}$ to $J_{\text{Fe-Fe}}$. The absolute topological charges are indicated in the color bar, and the ferromagnetic (FM, single domain), isolated-skyrmion (Sk), and skyrmionic (SkP) phases are labeled. In all simulations, we considered $T = 10^{-3}$ K.

identified as a key ingredient for the emergence of complex structures in frustrated magnets [95].

IV. CONCLUSIONS

We investigated the electronic and magnetic properties of Pd/Fe/Ir(111) and Pd/Co/Ir(111) using a combination of first-principles calculations and spin-dynamics simulations, aiming to explain their contrasting magnetic behaviors. For Pd/Fe/Ir(111), we obtained that the ground state is characterized by a noncollinear spin arrangement, in which both exchange and DMI have, simultaneously, significant roles. In particular, the emergent FM-AFM magnetic frustration present on the Fe-Fe exchange interactions is not sufficient to drive, alone, the Pd/Fe/Ir(111) bilayer into a noncollinear ground-state configuration, but leads to a metastable one. In turn, the Pd/Fe/Ir(111) DMI first-neighbor vectors, $\vec{D}_{ij}^{\text{1st}}$, exhibit an almost contrary behavior compared with Pd/Co/Ir(111), although both present a long-range influence, particularly driven by the D_y (in-plane) component. Due to this long-range nature of J_{ij} and $\vec{D}_{ij}$, the correct Pd/Fe/Ir(111) noncollinear states are only achieved with the consideration of, at least, fourth-neighbor interactions. Nevertheless, in the case of Pd/Co/Ir(111), these further-neighbor interactions are not sufficient to change the magnetic behavior from the simple FM (single-domain) configuration. In order to unravel this puzzle, by performing state-of-the-art *in silico* simulations, the original Pd/Co/Ir(111) $\vec{D}_{ij}$ and J_{ij} parameters were separately tuned to match the ones of Pd/Fe/Ir(111) and higher magnitudes. Interestingly, we found conditions for the emergence of the SkP in the originally FM single-domain Pd/Co/Ir(111), by rotating the DMI vectors or inducing a FM-AFM competition in the exchange interactions.

The *ab initio* J_{ij} and DMI behaviors have been shown to exhibit a simple rigid-band-like model nature. Among the most important effects, by switching the Fermi level to higher energies, the extra minority 3d electron in Co (with respect to Fe) is responsible for the emergence of a relevant AFM $J_{\text{Fe-Fe}}^{\text{3rd}}$ and a more in-plane $\vec{D}_{\text{Fe-Fe}}^{\text{1st}}$.

The present deep investigation contributes to the understanding of the origin of the noncollinear magnetism (and skyrmions) in Pd/Fe/Ir(111) but not in Pd/Co/Ir(111). Moreover, it also opens avenues to the study of conditions for the emergence of skyrmions in nonskyrmionic magnetic thin films.

ACKNOWLEDGMENTS

H.M.P. and A.B.K. acknowledge financial support from CAPES, CNPq, and FAPESP, Brazil. A.B. acknowledges eSSENCE. I.P.M. acknowledges financial support from CAPES, Finance Code 001, Process No. 88882.332894/2018-01, and the Institutional Program of Overseas Sandwich Doctorate, Process No. 88881.187258/2018-01. The calculations were performed at the computational facilities of the HPC-USP/CENAPAD-UNICAMP (Brazil), at the National Laboratory for Scientific Computing (LNCC/MCTI, Brazil), and at the Swedish National Infrastructure for Computing (SNIC).

---

[1] S. Holzberger, T. Schuh, S. Blügel, S. Lounis, and W. Wulfhekel, Phys. Rev. Lett. **110**, 157206 (2013).
[2] S. Lounis, P. H. Dederichs, and S. Blügel, Phys. Rev. Lett. **101**, 107204 (2008).
[3] R. N. Igarashi, A. B. Klautau, R. B. Muniz, B. Sanyal, and H. M. Petrilli, Phys. Rev. B **85**, 014436 (2012).
[4] M. S. Ribeiro, G. B. Corrêa, A. Bergman, L. Nordström, O. Eriksson, and A. B. Klautau, Phys. Rev. B **83**, 014406 (2011).

[5] R. N. Igarashi, I. P. Miranda, L. T. F. Eleno, A. B. Klautau, and H. M. Petrilli, J. Phys.: Condens. Matter **28**, 326001 (2016).
[6] S. Lounis, J. Phys.: Condens. Matter **26**, 273201 (2014).
[7] M. M. Bezerra-Neto, M. S. Ribeiro, B. Sanyal, A. Bergman, R. B. Muniz, O. Eriksson, and A. B. Klautau, Sci. Rep. **3**, 3054 (2013).
[8] S. H. Phark, J. A. Fischer, M. Corbetta, D. Sander, K. Nakamura, and J. Kirschner, Nat. Commun. **5**, 5183 (2014).
[9] R. Cardias, M. M. Bezerra-Neto, M. S. Ribeiro, A. Bergman, A. Szilva, O. Eriksson, and A. B. Klautau, Phys. Rev. B **93**, 014438 (2016).
[10] A. Fert, N. Reyren, and V. Cros, Nat. Rev. Mater. **2**, 17031 (2017).
[11] R. Wiesendanger, Nat. Rev. Mater. **1**, 16044 (2016).
[12] N. Romming, C. Hanneken, M. Menzel, J. E. Bickel, B. Wolter, K. von Bergmann, A. Kubetzka, and R. Wiesendanger, Science **341**, 636 (2013).
[13] S. Mühlbauer, B. Binz, F. Jonietz, C. Pfleiderer, A. Rosch, A. Neubauer, R. Georgii, and P. Böni, Science **323**, 915 (2009).
[14] J. Sampaio, V. Cros, S. Rohart, A. Thiaville, and A. Fert, Nat. Nanotechnol. **8**, 839 (2013).
[15] X. Zhang, M. Ezawa, and Y. Zhou, Sci. Rep. **5**, 9400 (2015).
[16] N. S. Kiselev, A. N. Bogdanov, R. Schäfer, and U. K. R. Ler, J. Phys. D: Appl. Phys. **44**, 392001 (2011).
[17] S. Heinze, K. von Bergmann, M. Menzel, J. Brede, A. Kubetzka, R. Wiesendanger, G. Bihlmayer, and S. Blügel, Nat. Phys. **7**, 713 (2011).
[18] M. Hervé, B. Dupé, R. Lopes, M. Böttcher, M. D. Martins, T. Balashov, L. Gerhard, J. Sinova, and W. Wulfhekel, Nat. Commun. **9**, 1015 (2018).
[19] I. E. Dzyaloshinskii, J. Phys. Chem. Solids **4**, 241 (1958).
[20] T. Moriya, Phys. Rev. **120**, 91 (1960).
[21] A. Bergman, A theoretical study of magnetism in nanostructured materials, Ph.D. thesis, Uppsala University, 2006.
[22] T. Okubo, S. Chung, and H. Kawamura, Phys. Rev. Lett. **108**, 017206 (2012).
[23] L. Rózsa, A. Deák, E. Simon, R. Yanes, L. Udvardi, L. Szunyogh, and U. Nowak, Phys. Rev. Lett. **117**, 157205 (2016).
[24] P. Jadaun, L. F. Register, and S. K. Banerjee, npj Comput. Mater. **6**, 88 (2020).
[25] N. Romming, A. Kubetzka, C. Hanneken, K. von Bergmann, and R. Wiesendanger, Phys. Rev. Lett. **114**, 177203 (2015).
[26] J. Spethmann, E. Y. Vedmedenko, R. Wiesendanger, A. Kubetzka, and K. von Bergmann, Commun. Phys. **5**, 19 (2022).
[27] L. Rózsa, E. Simon, K. Palotás, L. Udvardi, and L. Szunyogh, Phys. Rev. B **93**, 024417 (2016).
[28] E. Simon, K. Palotás, L. Rózsa, L. Udvardi, and L. Szunyogh, Phys. Rev. B **90**, 094410 (2014).
[29] C. Hanneken, F. Otte, A. Kubetzka, B. Dupé, N. Romming, K. von Bergmann, R. Wiesendanger, and S. Heinze, Nat. Nanotechnol. **10**, 1039 (2015).
[30] M. Böttcher, S. Heinze, S. Egorov, J. Sinova, and B. Dupé, New J. Phys. **20**, 103014 (2018).
[31] B. Dupé, M. Hoffmann, C. Paillard, and S. Heinze, Nat. Commun. **5**, 4030 (2014).
[32] L. V. Dzemiantsova, M. Hortamani, C. Hanneken, A. Kubetzka, K. von Bergmann, and R. Wiesendanger, Phys. Rev. B **86**, 094427 (2012).
[33] C. Back, V. Cros, H. Ebert, K. Everschor-Sitte, A. Fert, M. Garst, T. Ma, S. Mankovsky, T. Monchesky, M. Mostovoy, N. Nagaosa, S. S. P. Parkin, C. Pfleiderer, N. Reyren, A. Rosch, Y. Taguchi, Y. Tokura, K. von Bergmann, and J. Zang, J. Phys. D: Appl. Phys. **53**, 363001 (2020).
[34] S. Mankovsky, E. Simon, S. Polesya, A. Marmodoro, and H. Ebert, Phys. Rev. B **104**, 174443 (2021).
[35] H. Yang, O. Boulle, V. Cros, A. Fert, and M. Chshiev, Sci. Rep. **8**, 12356 (2018).
[36] N. S. Gusev, A. V. Sadovnikov, S. A. Nikitov, M. V. Sapozhnikov, and O. G. Udalov, Phys. Rev. Lett. **124**, 157202 (2020).
[37] L. Desplat, S. Meyer, J. Bouaziz, P. M. Buhl, S. Lounis, B. Dupé, and P.-A. Hervieux, Phys. Rev. B **104**, L060409 (2021).
[38] T. Srivastava, M. Schott, R. Juge, V. Krizakova, M. Belmeguenai, Y. Roussigné, A. Bernand-Mantel, L. Ranno, S. Pizzini, S.-M. Chérif, A. Stashkevich, S. Auffret, O. Boulle, G. Gaudin, M. Chshiev, C. Baraduc, and H. Béa, Nano Lett. **18**, 4871 (2018).
[39] S. Paul and S. Heinze, npj Comput. Mater. **8**, 105 (2022).
[40] P. R. Peduto, S. Frota-Pessôa, and M. S. Methfessel, Phys. Rev. B **44**, 13283 (1991).
[41] S. Frota-Pessôa, Phys. Rev. B **46**, 14570 (1992).
[42] A. Bergman, L. Nordström, A. B. Klautau, S. Frota-Pessôa, and O. Eriksson, Phys. Rev. B **73**, 174434 (2006).
[43] A. Bergman, L. Nordström, A. B. Klautau, S. Frota-Pessôa, and O. Eriksson, Phys. Rev. B **75**, 224425 (2007).
[44] A. Bergman, L. Nordström, A. B. Klautau, S. Frota-Pessôa, and O. Eriksson, Surf. Sci. **600**, 4838 (2006).
[45] O. K. Andersen, Phys. Rev. B **12**, 3060 (1975).
[46] R. Haydock, in *Solid State Physics*, edited by H. Ehrenreich, F. Seitz, and D. Turnbull (Academic Press, New York, 1980).
[47] U. von Barth and L. Hedin, J. Phys. C: Solid State Phys. **5**, 1629 (1972).
[48] N. Beer and D. G. Pettifor, *The Electronic Structure of Complex Systems*, edited by W. Temmermann and P. Phariseau (Plenum, New York, 1984).
[49] A. Liechtenstein, M. Katsnelson, V. Antropov, and V. Gubanov, J. Magn. Magn. Mater. **67**, 65 (1987).
[50] S. Frota-Pessôa, R. B. Muniz, and J. Kudrnovský, Phys. Rev. B **62**, 5293 (2000).
[51] A. Szilva, D. Thonig, P. F. Bessarab, Y. O. Kvashnin, D. C. M. Rodrigues, R. Cardias, M. Pereiro, L. Nordström, A. Bergman, A. B. Klautau, and O. Eriksson, Phys. Rev. B **96**, 144413 (2017).
[52] R. Cardias, A. Szilva, M. Bezerra-Neto, M. Ribeiro, A. Bergman, Y. O. Kvashnin, J. Fransson, A. Klautau, O. Eriksson, and L. Nordström, Sci. Rep. **10**, 20339 (2020).
[53] M. Gutzeit, S. Haldar, S. Meyer, and S. Heinze, Phys. Rev. B **104**, 024420 (2021).
[54] N. W. Ashcroft and N. D. Mermin, *Solid State Physics* (Saunders College, Philadelphia, 1976).
[55] B. Skubic, J. Hellsvik, L. Nordström, and O. Eriksson, J. Phys.: Condens. Matter **20**, 315203 (2008).
[56] O. Eriksson, A. Bergman, L. Bergqvist, and J. Hellsvik, *Atomistic Spin Dynamics: Foundations and Applications* (Oxford University Press, Oxford, 2017).
[57] S. Rohart, J. Miltat, and A. Thiaville, Phys. Rev. B **93**, 214412 (2016).
[58] I. S. Lobanov, H. Jónsson, and V. M. Uzdin, Phys. Rev. B **94**, 174418 (2016).

[59] G. Guo, W. Temmerman, and H. Ebert, J. Phys.: Condens. Matter **3**, 8205 (1991).
[60] P. Giannozzi, O. Andreussi, T. Brumme, O. Bunau, M. B. Nardelli, M. Calandra, R. Car, C. Cavazzoni, D. Ceresoli, M. Cococcioni, N. Colonna, I. Carnimeo, A. Dal Corso, S. de Gironcoli, P. Delugas, R. A. DiStasio Jr, A. Ferretti, A. Floris, G. Fratesi, G. Fugallo *et al.*, J. Phys.: Condens. Matter **29**, 465901 (2017).
[61] P. Giannozzi, S. Baroni, N. Bonini, M. Calandra, R. Car, C. Cavazzoni, D. Ceresoli, G. L. Chiarotti, M. Cococcioni, I. Dabo, A. Dal Corso, S. de Gironcoli, S. Fabris, G. Fratesi, R. Gebauer, U. Gerstmann, C. Gougoussis, A. Kokalj, M. Lazzeri, L. Martin-Samos *et al.*, J. Phys.: Condens. Matter **21**, 395502 (2009).
[62] A. Urru and A. Dal Corso, Phys. Rev. B **100**, 045115 (2019).
[63] H. J. Monkhorst and J. D. Pack, Phys. Rev. B **13**, 5188 (1976).
[64] S. Kirkpatrick, C. D. Gelatt, and M. P. Vecchi, Science **220**, 671 (1983).
[65] B. Berg and M. Lüscher, Nucl. Phys. B. **190**, 412 (1981).
[66] W. Weber, D. A. Wesner, G. Güntherodt, and U. Linke, Phys. Rev. Lett. **66**, 942 (1991).
[67] S. Polesya, S. Mankovsky, O. Sipr, W. Meindl, C. Strunk, and H. Ebert, Phys. Rev. B **82**, 214409 (2010).
[68] B. Dupé, G. Bihlmayer, M. Böttcher, S. Blügel, and S. Heinze, Nat. Commun. **7**, 11779 (2016).
[69] E. Sjöstedt and L. Nordström, Phys. Rev. B **66**, 014447 (2002).
[70] R. Lizárraga, L. Nordström, L. Bergqvist, A. Bergman, E. Sjöstedt, P. Mohn, and O. Eriksson, Phys. Rev. Lett. **93**, 107205 (2004).
[71] R. Cardias, A. Szilva, A. Bergman, I. Di Marco, M. Katsnelson, A. Lichtenstein, L. Nordström, A. Klautau, O. Eriksson, and Y. O. Kvashnin, Sci. Rep. **7**, 4058(2017).
[72] M. A. Ruderman and C. Kittel, Phys. Rev. **96**, 99 (1954).
[73] T. Kasuya, Prog. Theor. Phys. **16**, 45 (1956).
[74] K. Yosida, Phys. Rev. **106**, 893 (1957).
[75] A. A. Khajetoorians, M. Steinbrecher, M. Ternes, M. Bouhassoune, M. dos Santos Dias, S. Lounis, J. Wiebe, and R. Wiesendanger, Nat. Commun. **7**, 10620 (2016).
[76] A. Fert and P. M. Levy, Phys. Rev. Lett. **44**, 1538 (1980).
[77] A. Crépieux and C. Lacroix, J. Magn. Magn. Mater. **182**, 341 (1998).
[78] A. Belabbes, G. Bihlmayer, F. Bechstedt, S. Blügel, and A. Manchon, Phys. Rev. Lett. **117**, 247202 (2016).
[79] P. C. Carvalho, I. P. Miranda, A. B. Klautau, A. Bergman, and H. M. Petrilli, Phys. Rev. Materials **5**, 124406 (2021).
[80] S. Rohart and A. Thiaville, Phys. Rev. B **88**, 184422 (2013).
[81] S. Polesya, S. Mankovsky, S. Bornemann, D. Ködderitzsch, J. Minár, and H. Ebert, Phys. Rev. B **89**, 184414 (2014).
[82] A. Fert, V. Cros, and J. Sampaio, Nat. Nanotechnol. **8**, 152 (2013).
[83] P. Lindner, L. Bargsten, S. Kovarik, J. Friedlein, J. Harm, S. Krause, and R. Wiesendanger, Phys. Rev. B **101**, 214445 (2020).
[84] P. F. Bessarab, G. P. Müller, I. S. Lobanov, F. N. Rybakov, N. S. Kiselev, H. Jónsson, V. M. Uzdin, S. Blügel, L. Bergqvist, and A. Delin, Sci. Rep. **8**, 3433 (2018).
[85] I. P. Miranda, A. B. Klautau, A. Bergman, D. Thonig, H. M. Petrilli, and O. Eriksson, Phys. Rev. B **103**, L220405 (2021).
[86] A. Bisig, C. A. Akosa, J.-H. Moon, J. Rhensius, C. Moutafis, A. von Bieren, J. Heidler, G. Kiliani, M. Kammerer, M. Curcic, M. Weigand, T. Tyliszczak, B. Van Waeyenberge, H. Stoll, G. Schütz, K.-J. Lee, A. Manchon, and M. Kläui, Phys. Rev. Lett. **117**, 277203 (2016).
[87] L. Rózsa, J. Hagemeister, E. Y. Vedmedenko, and R. Wiesendanger, Phys. Rev. B **98**, 100404(R) (2018).
[88] S. Buhrandt and L. Fritz, Phys. Rev. B **88**, 195137 (2013).
[89] C. M. Schneider, P. Bressler, P. Schuster, J. Kirschner, J. J. de Miguel, and R. Miranda, Phys. Rev. Lett. **64**, 1059 (1990).
[90] S. von Malottki, P. F. Bessarab, S. Haldar, A. Delin, and S. Heinze, Phys. Rev. B **99**, 060409(R) (2019).
[91] X. S. Wang, H. Y. Yuan, and X. R. Wang, Commun. Phys. **1**, 31(2018).
[92] A. Kubetzka, C. Hanneken, R. Wiesendanger, and K. Von Bergmann, Phys. Rev. B **95**, 104433 (2017).
[93] F. N. Rybakov and N. S. Kiselev, Phys. Rev. B **99**, 064437 (2019).
[94] M. Ležaić, P. Mavropoulos, and S. Blügel, Appl. Phys. Lett. **90**, 082504 (2007).
[95] S. Hayami, S.-Z. Lin, and C. D. Batista, Phys. Rev. B **93**, 184413 (2016).